buildings

MDPI

Article

Fluid Flow Modeling and Experimental Investigation on a Shear Thickening Fluid Damper

Shiwei Chen [1], Xiaojiao Fu [1], Peiling Meng [1], Lei Cheng [1,2], Lifang Wang [1,2] and Jing Yuan [1,2,*]

[1] School of Civil Engineering and Architecture, Chongqing University of Science and Technology, Chongqing 401331, China; 2013001@cqust.edu.cn (S.C.); 2022206096@cqust.edu.cn (X.F.); mpl638@163.com (P.M.); zrhd244@163.com (L.C.); 308207283@icould.com (L.W.)

[2] Chongqing Institute of Metrology and Quality Testing, Chongqing 402260, China

* Correspondence: yuanjing38@163.com

Abstract: Shear Thickening Fluid (STF) is a specialized high-concentration particle suspension capable of rapidly and reversibly altering its viscosity when exposed to sudden impacts. Consequently, STF-based dampers deliver a self-adaptive damping force and demonstrate significant potential for applications in structural vibration control. This study presents both a modeling and experimental investigation of a novel double-rod structured STF damper. Initially, a compound STF is formulated using silica particles as the dispersed phase and polyethylene glycol solution as the dispersing medium. The rheological properties of the STF are then experimentally evaluated. The STF's constitutive rheological behavior is described using the G-R model. Following this, the flow behavior of the STF within the damper's annular gap is explored, leading to the development of a two-dimensional axisymmetric fluid simulation model for the damper. Based on this model, the dynamic mechanism of the proposed STF damper is analyzed. Subsequently, the STF damper is optimally designed and subjected to experimental investigation using a dynamic testing platform under different working conditions. The experimental results reveal that the proposed STF damper, whose equivalent stiffness can achieve a nearly threefold change with excitation frequency and amplitude, exhibits good self-adaptive capabilities. By dividing the damper force into two parts: the frictional damping pressure drop, and the osmotic pressure drop generated by the "Jamming effect". A fitting model is proposed, and it aligns closely with the nonlinear performance of the STF damper.

Keywords: shear thickening fluid; smart damper; shear thickening fluid-based damper

Citation: Chen, S.; Fu, X.; Meng, P.; Cheng, L.; Wang, L.; Yuan, J. Fluid Flow Modeling and Experimental Investigation on a Shear Thickening Fluid Damper. *Buildings* **2024**, *14*, 3548. https://doi.org/10.3390/buildings14113548

Academic Editor: Fabrizio Gara

Received: 26 September 2024
Revised: 31 October 2024
Accepted: 4 November 2024
Published: 7 November 2024

1. Introduction

Dampers, as crucial devices in engineering for vibration reduction and buffering, possess the capabilities to dissipate and store vibrational energy in engineering structures, effectively mitigating issues such as structural fatigue, damage, collapse, and buckling caused by external dynamic excitations [1–4]. In recent years, researchers have developed various types of smart dampers with controllable damping and stiffness based on novel intelligent materials whose mechanical properties can change with external physical field excitations, including magnetorheological fluids [5], electrorheological fluids [6], magnetorheological elastomers [7], and shape memory alloys [8], etc. These novel dampers can alter their own dynamic characteristics according to the structural vibration state, significantly enhancing the safety and stability of engineering structures under various vibration conditions. Nevertheless, due to the requirement of external energy for these novel dampers to realize their controllable functions, they have the disadvantages of being bulky, having complex structures, and requiring external power sources, making them difficult to apply in field environments that require long-term power supply. Therefore, there is an urgent need for innovative smart dampers that possess energy-free features.

In recent years, the evolution of preparation theories for Shear Thickening Fluid (STF) has paved the way for the potential realization of energy-free smart dampers. STF materials, categorized as a quintessential non-Newtonian fluid, comprise a suspension medium with microscopic particles dispersed within [9,10]. Upon exposure to shear forces, the interplay of relative friction, collisions, chemical bond restructuring, and alterations in particle configurations among these microscopic constituents manifests as a pronounced increase in the material's apparent viscosity in response to varying shear rates [11]. Scholarly investigations have elucidated that factors such as the choice of dispersed particles [12–15], their concentration [16,17], size [18,19], along with the nature of the dispersion medium and additives [14,20], exert profound influences on the shear thickening behavior exhibited by the material. Through meticulous modulation of these parameters during the STF preparation process, the material's apparent viscosity can be tuned to exhibit variations up to 1000-fold in response to external shear rate changes [15]. This remarkable capacity to adjust its viscosity across significant magnitudes without necessitating energy input positions STF as an emergent focal point within the realm of engineering vibration mitigation.

Research on applying STF (shear-thickening fluid) to liquid dampers can be traced back to the work of Hleber's team [21], who developed a vibration damping device based on STF materials, where the feedback force increases with the frequency of external excitation. Following this, Laun's group [22] proposed an intelligent damper design based on STF materials. In recent years, scholars have begun improving material compositions, resulting in reports of STF dampers with varying dynamic properties [23–25]. For example, Zhang XZ et al. [26] designed and fabricated a novel STF damper using STF material composed of nanoscale SiO_2 mixed with an ethylene glycol solution. Zhou et al. [27] reported an STF damper based on modified polystyrene discrete phases, whose equivalent stiffness can rapidly increase with the external load frequency. Overall, compared to other field-induced smart dampers, STF dampers require no energy input or sensing systems to achieve rapid dynamic changes. This feature demonstrates significant potential in vibration reduction applications for large outdoor structures, such as overhead high-voltage transmission lines.

At present, research on STF dampers is still in its early stages, with existing studies primarily focusing on changes in viscous damping. Apart from the ref. [27], There are few reports on STF dampers capable of achieving rapid and significant changes in equivalent stiffness. Furthermore, the optimization of damper structural parameters based on the rheological properties of STF materials, aiming to ultimately achieve the utmost variation in its equivalent stiffness, still necessitates comprehensive and thorough investigation. Therefore, this paper presents the development of a composite STF material based on a mixture of SiO_2 and a compound polyethylene glycol solution. By testing the rheological behavior of the material, the strain-rate-sensitive region was identified. Using a combination of FEM simulation and mechanical design, the internal flow field distribution within the annular gap was investigated, leading to the design and prototyping of an STF damper. Experimental tests were conducted using a dynamic testing platform, and the results demonstrate that the proposed STF damper can achieve a nearly threefold change in equivalent stiffness. This novel STF-based damper is expected to exhibit high stiffness when subjected to impact loads, maintaining structural stability, while offering significant flexibility under low-frequency loads to reduce internal fatigue stress, showing great potential for applications in fields such as seismic mitigation for structures and wind vibration suppression for power transmission lines.

2. The Preparation and Rheological Testing of STF Samples

2.1. Preparation of STF Samples

Considering the chemical and physical stability requirements as well as the cost demands for the damper's STF material, the STF in this study employs silicon dioxide (SiO_2) with a diameter of 500 nm (procured from Sinopharm Chemical Reagent Co., Ltd., Shanghai, China) as the dispersed phase, and a compounded polyethylene glycol (PEG) solution (PEG200:PEG400 = 1:2, purchased from Xilong Scientific Co., Ltd., Shenzhen,

China) as the dispersing medium. The detailed preparation process of the STF material is shown in Figure 1a. As illustrated in Figure 1a, the SiO_2 particles are first placed in a blast drying oven at 70 °C for 30 min to dry and dehumidify, ensuring that the dispersed phase particles remain dry. Then, the SiO_2 particles are mixed with the compounded polyethylene glycol solution at a mass ratio of 1:3, and anhydrous ethanol (purchased from Sinopharm Chemical Reagent Co., Ltd., Shanghai, China) is added to form a high-concentration particle suspension. Subsequently, the suspension is stirred for 60 min using an electric stirrer to ensure that the SiO_2 particles are uniformly dispersed in the dispersing medium. The suspension is then transferred to a beaker and placed in an ultrasonic cleaner for 20 min, followed by placement in an electric vacuum drying oven for 120 min, completing the STF material preparation.

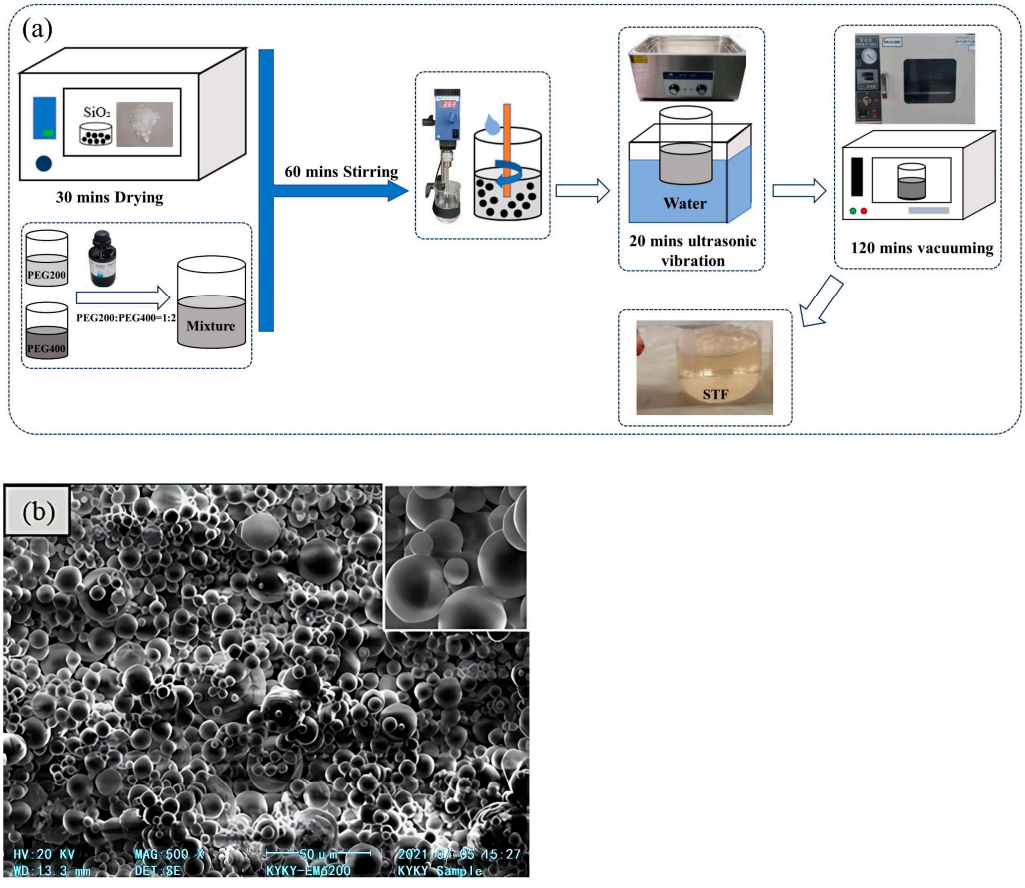

Figure 1. The fabrication of the STF material (**a**) The preparation process of STF material (**b**) The SEM picture of SiO_2.

Additionally, Figure 1b shows the SEM picture of the STF material. From the picture, it can be observed that the SiO_2 particles have smooth surfaces and regular shapes, which aids their uniform dispersion in the polyethylene glycol medium. This allows the material to exhibit low viscosity at low shear rates while demonstrating Newtonian fluid characteristics [28]. Moreover, the particle clusters show a significant degree of agglomeration, which helps to increase inter-particle friction within the clusters. This enhances the likelihood of jamming at high shear rates, thus enabling the liquid-solid phase transition region.

2.2. Rheological Testing of STF Samples

At a stable ambient temperature of 20 °C, the rheological properties of the prepared STF material were meticulously evaluated using the compact modular rheometer (MCR102, Anton Paar Company, Duisburg, Germany). The experiment adhered to the manufacturer's recommended rheological testing protocol, and a pre-shear process was conducted before

initiating the test. During the oscillatory shear rheological test, the shear rate was varied within a range of 1 to 100 1/s. The corresponding test results are presented in Figure 2.

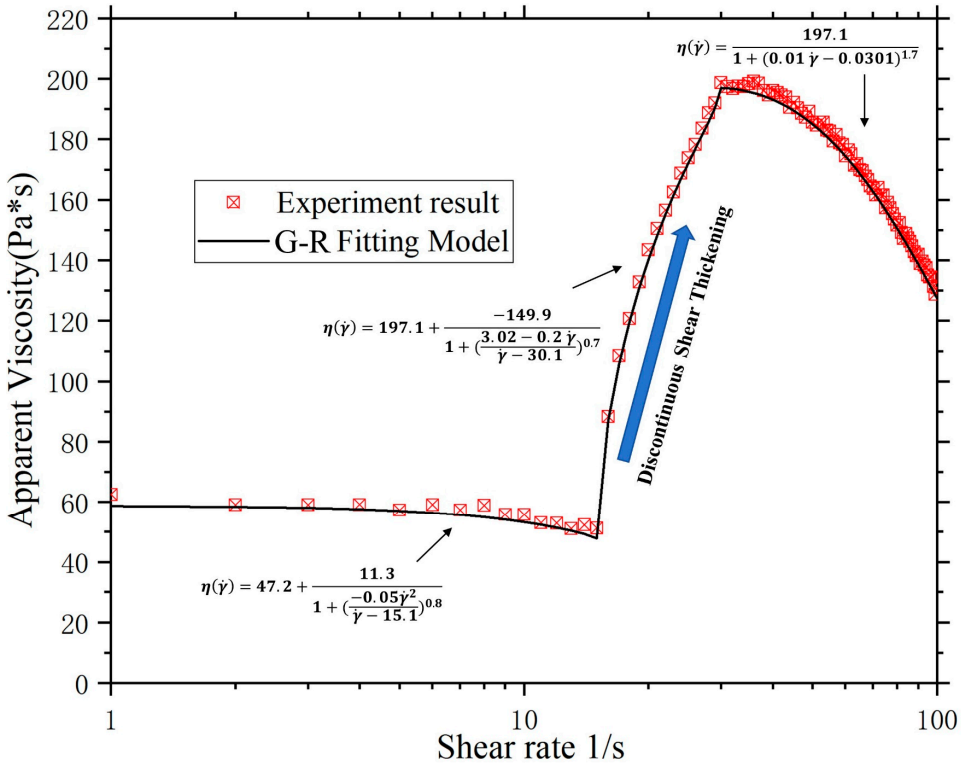

Figure 2. The rheological properties of the STF.

As shown in Figure 2, the critical shear rate for the compounded STF material's shear thickening behavior occurs at 15.1 1/s. Before the shear rate reaches this value, the fluid's viscosity changes insignificantly, and it can be approximately considered as a Newtonian fluid, with an apparent viscosity of 62.5 Pa·s. Upon reaching the critical shear rate, a marked discontinuous shear thickening phenomenon was observed, with the apparent viscosity at 47.8 Pa·s. The viscosity rapidly increased from 47.8 Pa·s to 197.2 Pa·s, with a change rate of 412%, clearly demonstrating discontinuous shear thickening.

As the shear rate continued to rise and reached 30.1 1/s, the material yielded, and the apparent viscosity began to decrease with increasing shear rate. By the time the shear rate reached 100 1/s, the viscosity dropped from 197.2 Pa·s to 132.1 Pa·s, exhibiting shear thinning behavior. Therefore, to design a self-adaptive smart damper with a large range of variable damping force, it is essential to ensure that the STF material inside the damper operates within the shear thickening state, specifically maintaining a shear rate between 15.1 1/s to 30.1 1/s during damper operation.

Based on the previous analysis, the viscosity variation in STF materials can be roughly categorized into three regions: the low-shear rate region, the shear thickening region, and the shear thinning region. Galindo-Rosales [29] provided a phenomenological model for these three regions, and its expression is as follows:

$$\begin{cases} \eta(\dot{\gamma}) = \eta_c + \frac{(\eta_0-\eta_c)}{1+\left[K_1(\frac{\dot{\gamma}^2}{\dot{\gamma}-\dot{\gamma}_c})\right]^{n_1}} & for\ \dot{\gamma} \le \dot{\gamma}_c \\ \eta(\dot{\gamma}) = \eta_{max} + \frac{\eta_c-\eta_{max}}{1+\left[K_2(\frac{\dot{\gamma}-\dot{\gamma}_c}{\dot{\gamma}-\dot{\gamma}_{max}})\right]^{n_2}} & for\ \dot{\gamma}_c \le \dot{\gamma} \le \dot{\gamma}_{max} \\ \eta(\dot{\gamma}) = \frac{\eta_{max}}{1+\left[K_3(\dot{\gamma}-\dot{\gamma}_{max})\right]^{n_3}} & for\ \dot{\gamma}_{max} \le \dot{\gamma} \end{cases} \quad (1)$$

In the equation, η_0 represents the initial apparent viscosity of the shear thickening fluid, with a fitted value of 58.5 Pa·s; η_c is the minimum apparent viscosity of the shear thickening fluid, with a fitted value of 47.2 Pa·s; and η_{max} is the maximum viscosity of the shear thickening fluid, with a fitted value of 197.1 Pa·s. $\dot{\gamma}_c$ and $\dot{\gamma}_{max}$ represent the critical shear rates for the onset of shear thickening and shear thinning phenomena, respectively, with values of 15.1 1/s and 30.1 1/s. The parameters n_1, n_2, n_3, K_1, K_2, and K_3 are fitting constants, with values of 0.8, 0.7, 1.7, −0.05, −0.2, and 0.01, respectively. As shown in Figure 2, the G-R fitting model effectively captures the steady-state rheological properties of the compounded STF material reported in this study.

3. The Design and Simulation of STF Dampers

3.1. Designing of the STF Dampers

Considering the advantages of a double-rod structure, such as fewer seals and the loss of requirement for an air compensation chamber, a double-rod intermittent STF damper based on the compounded STF material is proposed. The schematic diagram, 3D models, and prototype are shown in Figure 3a, Figure 3b, and Figure 3c, respectively.

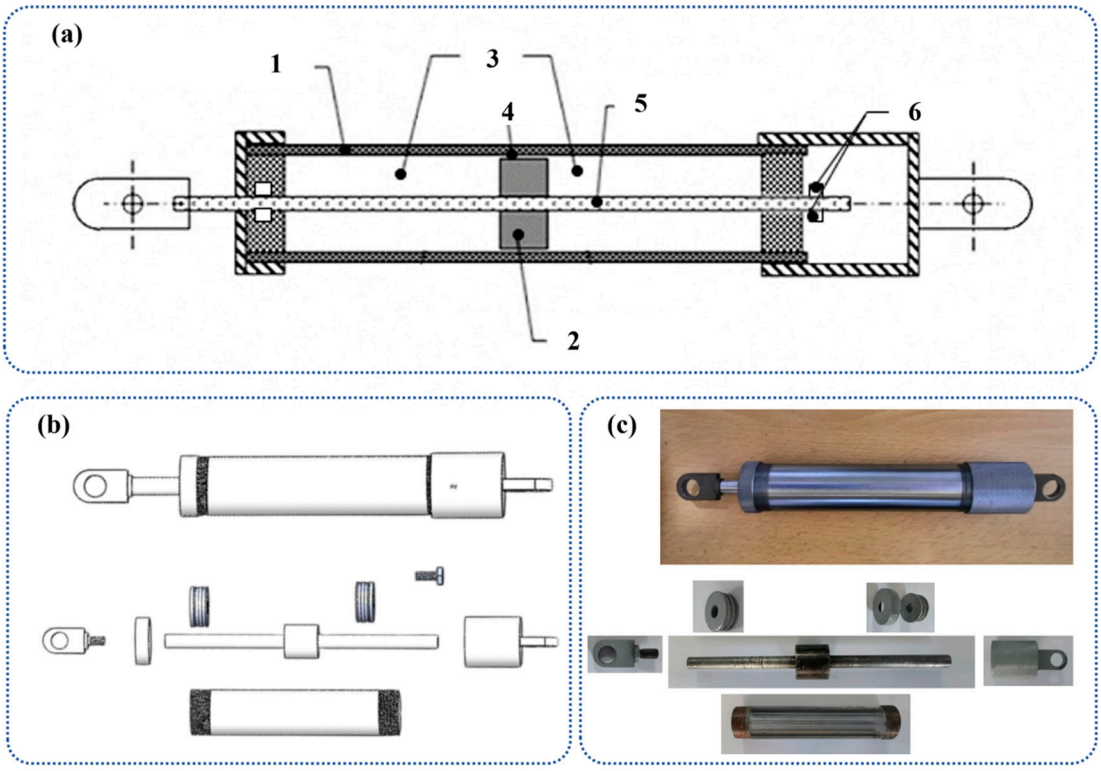

Figure 3. Designing of the STF damper (**a**) schematic, 1. Damper tube, 2. Piston head, 3. Cylinder chamber, 4. Annular gap, 5. Piston rod, 6. Seal rings (**b**) 3D model (**c**) Prototype.

As illustrated, the proposed STF damper primarily consists of front and rear end caps, a damper tube, and a piston rod. The damper tube and push rod (including the piston) are made of Q235 stainless steel. Inside the STF cylinder chamber, a piston rod (with piston) is installed. To ensure the smooth movement of the piston within the sealed cylinder chamber, sealing rings are placed above and below the piston rod, while the damper tube is sealed by the front and rear end caps. By adopting the double-rod structure, an annular gap is formed between the cylinder chamber and the piston.

The compounded STF material is filled into the cylinder chamber of the damper. When subjected to external loads, the push rod moves, causing the piston to compress the STF material within the annular gap. This forces the STF from the cylinder chamber on one side of the piston through the annular gap into the cylinder chamber on the other side of the

piston. During this process, as the piston movement speed changes, the apparent viscosity of the STF material also changes accordingly, resulting in variations in the damping force exerted on the piston rod. This ultimately leads to the damper filled with STF exhibiting a nonlinear dynamic property that changes with external loads. Considering the structural sealing and the overall machining complexity of the damper, the initial design dimensions of each component are listed in Table 1.

Table 1. Parameters of the proposed STF damper.

Parameters	Value (mm)
Diameter of push rod	15
Length of push rod	295
Length of piston	15
Diameter of piston	30–40
Outer diameter of damper	58
Wall thickness	4
Length of cylinder chamber	255
Diameter of cylinder chamber	54

3.2. Simulation and Optimization of the STF Damper

As shown in Figure 2, the STF material exhibits shear thickening behavior only within a suitable range of shear rates. Therefore, this section establishes a FEM model of the STF damper to analyze the shear rate of the STF in the annular gap. The goal is to ensure that the STF material operates at its optimal shear rate within the intermittent region of the impact load, ultimately completing the optimization of the piston diameter in the damper. The FEM model of the STF damper used in this study is shown in Figure 4. Based on the symmetry of the flow field inside the damper, a two-dimensional axisymmetric model is adopted, with the geometric central axis of the damper as the axis of symmetry. The model dimensions are provided in Table 1.

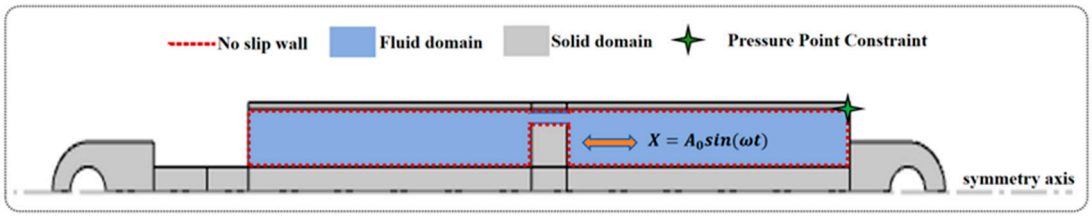

Figure 4. Flow Field Computation Model STF damper.

As shown in Figure 4, the flow field of the damper was simulated using the Laminar Flow Module of the commercial finite element software COMSOL Multiphysics 6.0. In the computation model, the cylinder chamber of the damper was defined as the fluid domain, while the other regions of the damper were set as solids. The interface between the fluid and solid domains was configured as a no-slip wall, and the upper-right corner of the fluid domain was set as a zero-pressure boundary. On this basis, the Lagrangian–Eulerian method was employed to simulate the cyclic motion of the STF damper under sinusoidal excitation. By incorporating a moving mesh module in the software, the fluid domain was set as a freely moving mesh domain, with the piston movement defined by the equation $X = A_0 sin(\omega t)$. And the density of the STF (Shear Thickening Fluid) in the fluid domain is set at 1.870 g/mm^3, while its dynamic viscosity, which varies based on the shear rate, is determined using fitting data from Equation (1).

Leveraging the developed model, Figure 5 meticulously depicts the average shear rate and its distribution within the STF-filled annular gap, under conditions where the piston diameter is 36 mm, the displacement amplitude is 3 mm, and the frequency is 5 Hz. The figure vividly illustrates that the piston's cyclic motion induces considerable shear

deformation within the STF in the annular gap, with the highest shear rate concentrated near the edges of the piston in the annular gap region. As the piston reaches its central position, the velocity attains its peak, resulting in a maximum shear rate at the periphery of the annular gap, signifying that the nonlinear shear thickening behavior of the STF will predominantly emerge in this region. Furthermore, Figure 5 reveals a periodic pattern in the average shear rate variation within the annular gap, closely corresponding to the oscillatory movement of the piston. The shear rate achieves its maximum value of 62.1 1/s when the piston displacement is at zero and diminishes to 0.1 1/s at the maximum displacement.

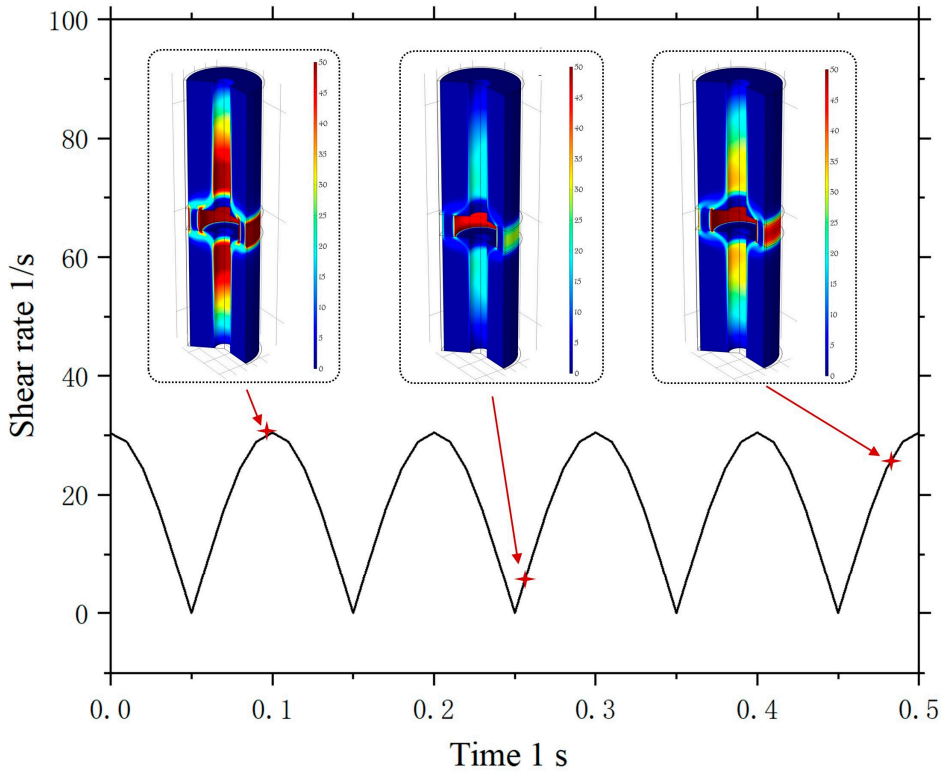

Figure 5. The average shear rate of STF in the annular gap when the damper subjected a A_0 = 3 mm, f = 5 Hz sine displacement excitation.

Building on the FEM model, Figure 6 demonstrates the variation in the amplitude of the average shear rate of the STF within the annular gap, as the piston diameter ranges from 30 to 40 mm, with a piston displacement amplitude of 3 mm and varying frequencies of 1, 3, and 5 Hz. The figure reveals a clear trend: as the piston diameter increases, the average shear rate of the STF escalates accordingly. Under the excitation of a 1 Hz sinusoidal displacement, the shear rate increases from 3.4 1/s to 11.9 1/s; when subjected to a 2 Hz excitation, it rises from 10.3 1/s to 35.9 1/s; and at 3 Hz excitation, it surges from 13 1/s to 55.9 1/s.

As depicted in Figure 2, the shear thickening behavior of the STF manifests within the shear rate range of 15.1 to 30.1 1/s. When the shear rate surpasses 30.1 1/s, the material experiences shear yielding and transitions into a shear thinning state, thereby diminishing the variable damping performance of the STF damper. Accordingly, as shown in Figure 6, with a piston diameter of 36 mm, the maximum average shear rate of the STF within the annular gap fluctuates between 5.3 and 30.1 1/s. This ensures that the average shear rate of the fluid within the annular gap resides in the optimal shear rate range, allowing the STF to exhibit low viscosity under low vibration energy excitation, which places the damper in a low damping state. This significantly mitigates alternating fatigue stress imposed on the structure. Conversely, under high vibration energy excitation, the fluid transitions into a shear thickening high-viscosity state, thereby amplifying the damper's damping force

and enhancing the structural stability. Accordingly, a piston with a diameter of 36 mm was selected for the fabrication of the STF damper prototype.

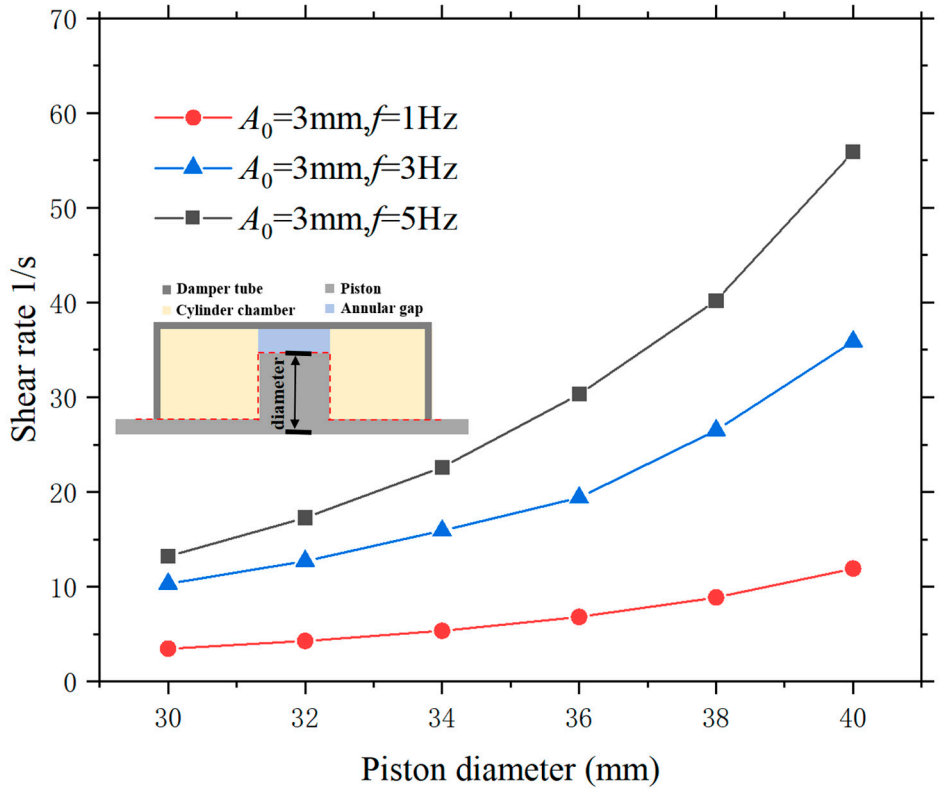

Figure 6. Amplitude variation of STF shear rate with piston diameter (30–40 mm) when the damper subjected a A_0 = 3 mm, f = 5 Hz sine displacement excitation.

4. The Dynamic Property of STF Dampers

4.1. Dynamic Testing of STF Damper

To investigate the dynamic properties of the STF damper, a dynamic testing platform was constructed. Figure 7 illustrates the experimental picture and its schematic diagram. As depicted in Figure 7a, the entire system comprises an electric loading device, a spatial adjustment frame, and fixture. The electric loading device integrates a high-precision planetary ball screw and a Shandong Bangce AC servo motor (PWD-10), capable of handling a maximum dynamic load of ±10 kN, with a dynamic frequency range of 0 to 10 Hz and an amplitude property of ±10 mm. The spatial adjustment frame includes a lifting beam, guide rails, and a lift cylinder to precisely adjust the height required for the STF damper experiments. The fixture, specifically designed in a "horn" shape to accommodate the structural configuration of the STF damper, provide efficient, accurate, and user-friendly testing capabilities. The damper is secured to the fixture through washers, which enhance the overall stability between the line clip and the fixture.

As illustrated in Figure 7b, the STF damper is firmly mounted onto the testing platform using a fixture. A force sensor is installed at the upper part of the platform to capture the output force, with the data collected and uniformly stored in a computer via a controller for seamless post-processing. The dynamic characteristic experiments on the STF damper were conducted using a sinusoidal excitation signal as the displacement input, with excitation frequencies set at 1 Hz, 3 Hz, and 5 Hz, and displacement amplitudes of 1 mm, 2 mm, and 3 mm. To provide a meaningful comparison, an ordinary particle suspension lacking shear thickening properties was introduced into the damper to form a control group, simulating a conventional viscous damper. The dynamic properties of this control damper were tested at a displacement amplitude of 3 mm, with frequencies of 1 Hz, 3 Hz, and 5 Hz, to compare against the STF damper under identical conditions.

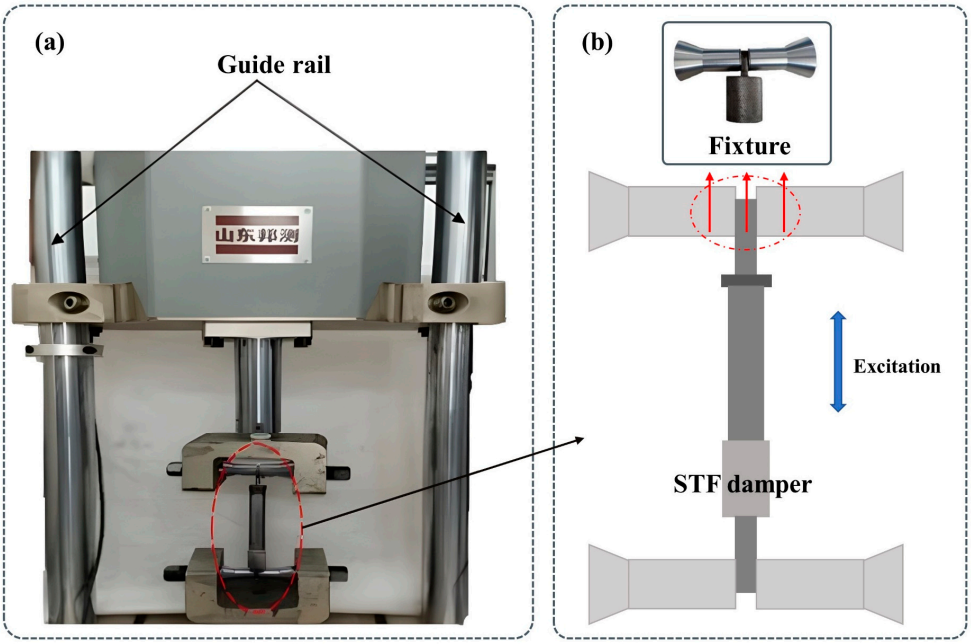

Figure 7. Dynamic testing platform of the STF damper (**a**) experimental picture (**b**) enlarged schematic diagram of the STF damper.

Figure 8 presents the force-displacement hysteresis curves for both the STF damper and the control damper under various frequencies and amplitudes. As illustrated in Figure 8a, the feedback force of the STF damper demonstrates heightened sensitivity to changes in excitation frequency and displacement amplitude, underscoring the pronounced rate-dependent nature of the dynamic properties exhibited by the shear thickening STF damper. At lower excitation frequencies, the piston velocity of the STF damper is relatively slow, leading to a significant overlap in the 1 Hz curve with a gentle slope, indicative of the STF damper's limited energy dissipation capability and correspondingly low output force at these frequencies.

However, as both the excitation frequency and amplitude increase, the rapid motion of the piston elevates the shear rate, ultimately surpassing the critical shear rate, which triggers a sharp escalation in the viscosity of the STF damper. As a result, the output force surges from 13 N to 58 N, representing an increase in more than four times compared to the output force at lower frequencies. Furthermore, as depicted in Figure 8b,c, the reduction in amplitude from 3 mm to 1 mm is accompanied by a marked contraction in the area of the hysteresis loops, indicating a substantial decrease in the damper's energy dissipation capacity per cycle. The observed narrowing of the curve width at lower amplitudes further highlights a reduced range of response forces, signifying a diminished control capacity of the damper in these conditions.

Figure 8d portrays the force-displacement hysteresis curves of the control group at a displacement amplitude of 3 mm. Much like the STF damper, the control group displays a pronounced sensitivity to frequency variations, with the amplitude of the damping force fluctuations expanding in tandem with increasing frequency. This effect is particularly notable at 5 Hz, where the force response becomes significantly more prominent. However, a closer examination of the curve's slope reveals that there is virtually no observable change in slope under displacement loading, indicating that the adjustable stiffness capability of this damper is exceedingly limited.

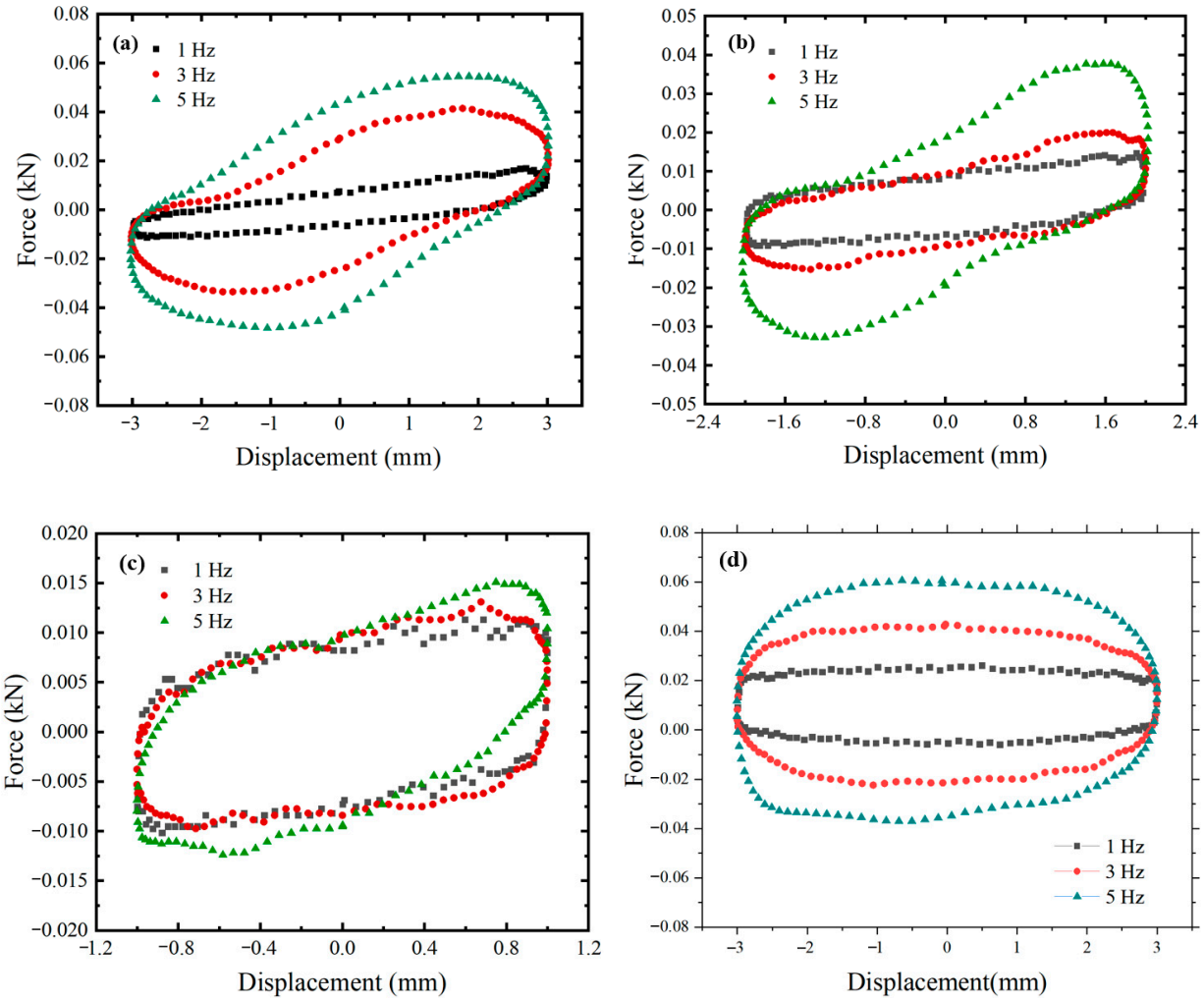

Figure 8. Force-displacement hysteresis curves at different frequencies and amplitudes (**a**) STF damper, A = 3 mm (**b**) STF damper, A = 2 mm (**c**) STF damper, A = 1 mm (**d**) Control group damper, A = 3 mm.

By employing Equations (2) and (3) to articulate the definitions of equivalent stiffness and viscous coefficient [27], one can compute the dynamic properties of both the STF damper and the control group damper.

$$k_e = (F_+ - F_-)/2A_{max} \tag{2}$$

$$c_e = w_d/\pi\omega A_0^2 \tag{3}$$

In the equation: F_+, F_- represent the output forces at the maximum piston displacement A_0, w_d denotes the energy dissipated during each cycle, and ω is the excitation angular frequency.

As depicted in Figure 9a, the control group damper exhibits an equivalent stiffness of zero under reciprocating loading conditions. In stark contrast, the equivalent stiffness of the STF damper undergoes a substantial increase with rising excitation frequency, ascending from 3.1 N/mm to 9.2 N/mm under dynamic excitation with a displacement amplitude of 3 mm. This phenomenon, which is also observed in reference [27], can be attributed to the "jamming effect" caused by the internal particles of the STF liquid as it flows through the annular gap [30]. During high-speed motion, friction and collisions occur among the dispersed particles within the STF material, ultimately leading to the formation of particle clusters. This process triggers a phase transition in the material at the macroscopic level,

causing it to shift from a liquid to a solid phase. As the piston moves, the deformation of the solid-phase STF material within the model causes the damper to exhibit elastic properties. With an increase in piston speed, the average shear rate of the STF material within the chamber rises, resulting in more STF material undergoing phase transition. Consequently, the STF damper exhibits variable stiffness characteristics that are intrinsically linked to the excitation frequency.

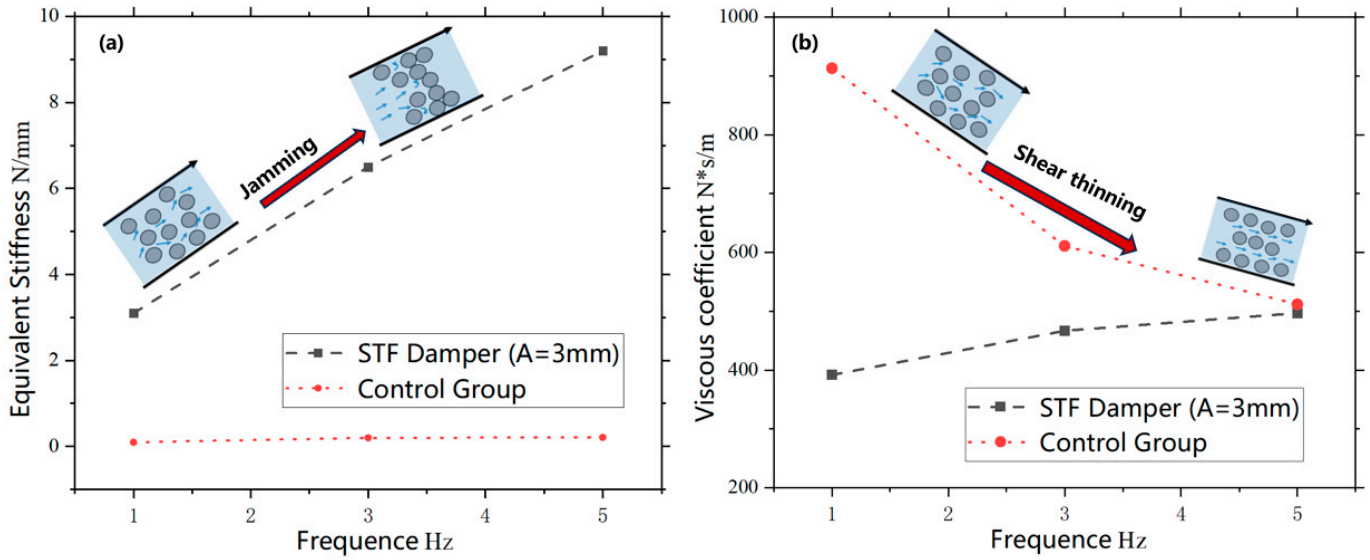

Figure 9. The dynamic properties of the proposed dampers, the blue arrows represent the trajectory of an infinitesimal fluid element, the black arrow represent the direction of fluid flow (**a**) Equivalent stiffness (**b**) Viscous coefficient.

Furthermore, as illustrated in Figure 9b, the viscous coefficient of the control group damper experiences a pronounced decline as the excitation frequency diminishes, plummeting from 913 N·s/m to 512 N·s/m, which signifies a clear shear thinning phenomenon. Conversely, the viscous coefficient of the STF damper exhibits a gradual increase in response to escalating excitation frequencies.

4.2. Nonlinear Fitting Model

As demonstrated in Figure 8, the dynamic properties of the STF damper are influenced by fluctuations in the frequency and amplitude of external excitation. However, employing both frequency and amplitude as fitting parameters for the equivalent stiffness and viscosity coefficient of the damper introduces the challenge of an excessive number of fitting variables. Consequently, this chapter will initially utilize the theory of non-Newtonian fluid dynamics to analyze the nonlinear behavior of the fluid within the STF damper. Building upon this foundational analysis, a quantitative assessment of the correlation between the dynamic properties of the STF damper and the parameters of the excitation load will be conducted, culminating in the establishment of a nonlinear fitting model aimed at accurately capturing the complex nonlinear dynamics of the STF damper.

This study posits that the STF is incompressible, continuous, homogeneous, and maintained in a laminar flow state, while disregarding both inertial and gravitational forces. The flow of the STF material within the annular gap is conceptualized as a one-dimensional gap flow distribution, as depicted in Figure 10a.

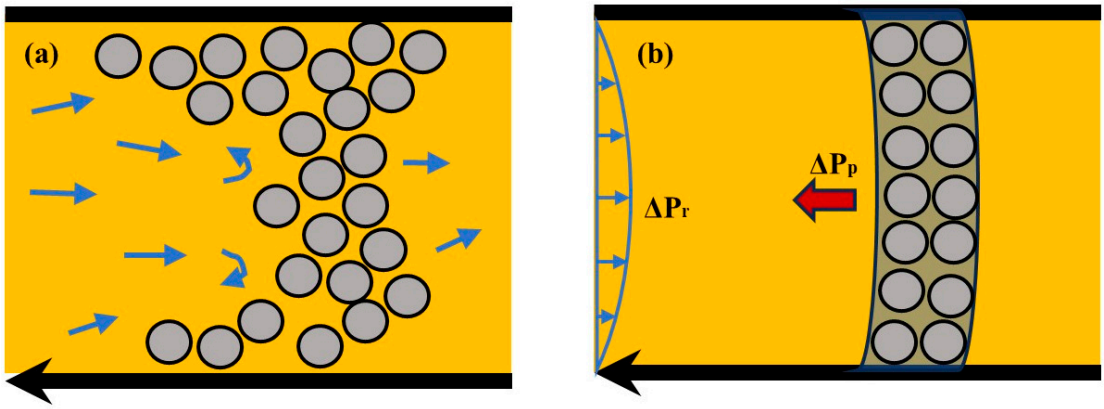

Figure 10. Fluid state between the gap of the damping spacer bar plate, the blue arrows represent the trajectory of an infinitesimal fluid element (**a**) Micro-scale particle blockage phenomenon (**b**) Flow model.

As depicted in Figure 10b, the feedback force F_f of the STF damper is intrinsically defined by two principal components: the frictional damping pressure drop ΔP_r that the STF material encounters while navigating the annular gap, and the osmotic pressure drop ΔP_p resulting from the "jamming effect". This relationship can be articulated mathematically as follows:

$$F_f = \Delta P_r + \Delta P_p \tag{4}$$

When the STF damper performs sinusoidal motion characterized by $A_0 sin(2\pi ft)$, the frictional damping pressure drop within the STF damper can be rigorously analyzed through the flow model established by parallel plate theory [31]. By employing the momentum equation for the fluid, the governing equation for the flow of the STF can be expressed as follows:

$$\frac{\partial \sigma}{\partial x} + \frac{\partial \tau}{\partial z} = \rho\left(\frac{\partial v_x}{\partial t} + v_x\frac{\partial v_x}{\partial x} + v_z\frac{\partial v_x}{\partial z}\right) \tag{5}$$

In the context of the equation, σ and τ represent the normal stress and shear stress of the STF liquid in the x-direction, respectively. Concurrently, v_x and v_z denote the flow velocities of the STF along the x and z axes, respectively, while ρ signifies the liquid density of the STF material. Considering that the fluid exhibits one-dimensional flow in the x-direction and neglecting the effects of inertial forces, Equation (4) can be succinctly simplified to:

$$\frac{\partial \sigma}{\partial x} + \frac{\partial \tau}{\partial z} = 0 \tag{6}$$

According to the definition of the pressure gradient, $dp/dx = -\partial\sigma/\partial x$. Thus, Equation (5) can be further simplified to:

$$\frac{\partial \tau}{\partial z} = \frac{dP_r}{dx} \tag{7}$$

In this equation, P_r represents the frictional damping pressure of the liquid. Upon integration, the result is:

$$\tau(z) = \frac{dP_r}{dx}z + C \tag{8}$$

According to the definition of viscosity, the relationship between shear stress and shear rate is as follows:

$$\tau(z) = \eta\frac{dv_x}{dz} \tag{9}$$

By jointly solving Equation (8) and Equation (7), integrating with respect to z, and subsequently applying the boundary conditions, the flow velocity of the STF material in the x-direction can be expressed as:

$$v_x = \begin{cases} -\frac{1}{2\eta}\frac{dP_r}{dx}\left[\frac{h}{4}^2 - \left(\frac{h}{2} - z\right)^2 - \dot{X}(t)\right] & (0 \le z < \frac{h}{2}) \\ -\frac{1}{2\eta}\frac{dP_r}{dx}\left[\frac{h}{4}^2 - \left(z - \frac{h}{2}\right)^2\right] & (\frac{h}{2} \le z < h) \end{cases} \tag{10}$$

According to the definition of volumetric flow rate:

$$\pi r \int_0^h v_x dz = S_p \, \dot{X}(t) \tag{11}$$

In this context, r denotes the radius of the parallel plate, equivalent to half the circumference of the annular gap, while S_p represents effective cross-sectional area of the STF. $X(t)$ corresponds to the shear displacement of the parallel plate (i.e., the piston), with $\dot{X}(t)$ indicating the shear rate of the parallel plate. By substituting Equations (8) and (9) into Equation (10), and applying $dP_r/dx = -\Delta P_r/l$ (under conditions of uniform laminar flow), the frictional damping pressure drop can be derived through integration [31].

$$\Delta P_r = \frac{12{S_p}^2 \dot{X}(t) L\eta}{\pi r h^3} + \frac{6 S_p \dot{X}(t) L\eta}{h^2} \tag{12}$$

In this equation, L denotes the length of the shear domain, and the aforementioned represents the frictional force arising from the flow of the STF liquid. The parameter η refers to the viscosity of the STF liquid. Moreover, at high shear rates, the particles within the STF become jammed in the shear zone, inducing a "jamming effect" that leads to solidification around the piston, which, on a macroscopic scale, triggers a phase transition in the STF liquid. To model this phenomenon, this study simplifies the post-phase-transition material as a simply supported beam undergoing bending deformation in the flow field. Consequently, the osmotic pressure drop in the liquid region, induced by the permeation of the elastic solidified phase, can be expressed as:

$$\Delta P_p = \frac{48EI}{h^3} X(t) + f_N sign(\dot{X}(t)) \tag{13}$$

In this equation, EI represents the equivalent shear stiffness, and f_N denotes the frictional force exerted by the piston on the "jammed" phase. By substituting Equations (12) and (13) into Equation (4), the damping force relationship for the STF damper can be derived as follows:

$$F = \left(\frac{12{S_p}^2 L}{\pi r h^3} + \frac{6 S_p L}{h^2}\right)\eta \dot{X}(t) + \frac{48EI}{h^3} X(t) + f_N sign(\dot{X}(t)) \tag{14}$$

In this equation, h, L, S_p and r represent the structural constants of the annular gap, while the STF viscosity η, equivalent shear stiffness EI and the frictional force f_N are related to the degree of "jamming" within the STF's internal micro particles. The "jamming" phenomenon of the particles is directly correlated with the peak piston velocity v_{max}. Therefore, the damping force model of the STF damper, as expressed in Equation (14), can be further simplified into the following phenomenological model:

$$F = c_e(v_{max})\dot{X}(t) + k_e(v_{max})X(t) + \mu_e(v_{max}) sign(\dot{X})$$

$$c_e = a + b v_{max} + c v_{max}^2$$

$$k_e = e + f v_{max} + g v_{max}^2$$

$$\mu_e = h + iv_{max} + jv_{max}^2 \tag{15}$$

In this equation, c_e and k_e denote the dynamic viscous and equivalent stiffness of the damper, respectively. Drawing from the experimental data, Figure 11 presents the relationship between these two parameters and the peak velocity of the piston motion.

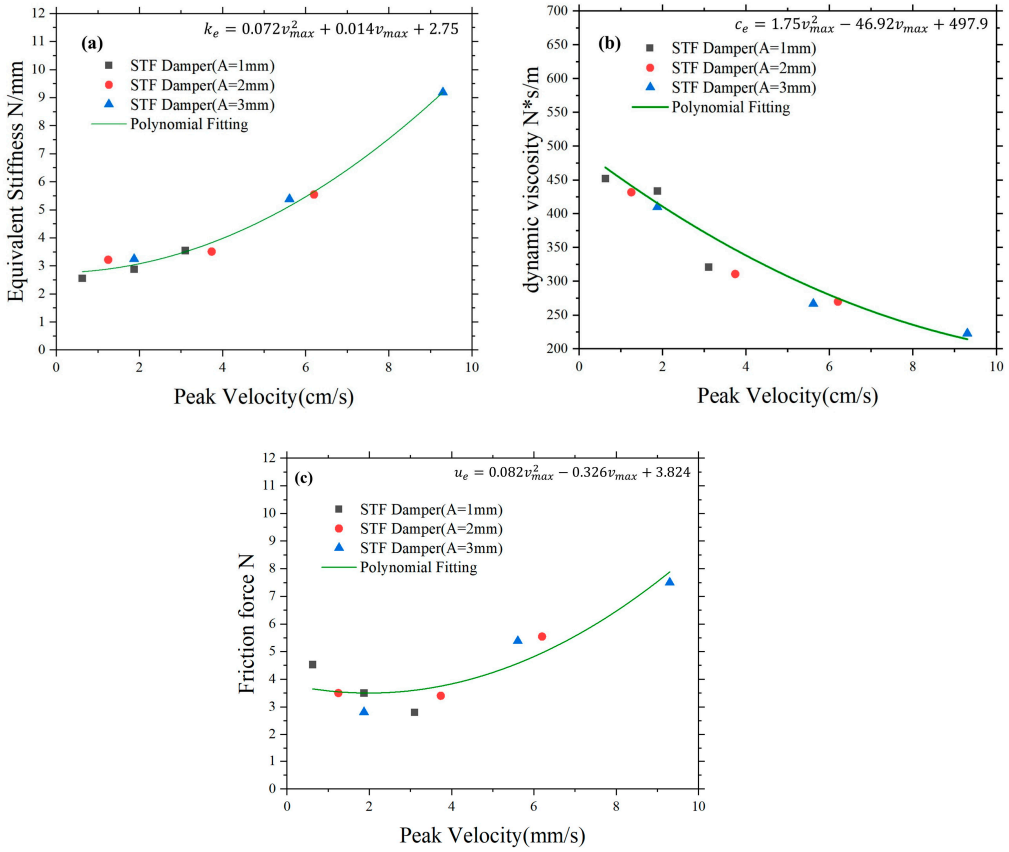

Figure 11. The dynamic properties of the proposed dampers (**a**) Equivalent stiffness, e = 2.75, f = 0.014, g = 0.072 (**b**) Dynamic viscous a = 497.9, b = −46.92, c = 1.75 (**c**) Friction force, h = 3.824, i = −0.326, j = 0.082.

As illustrated in Figure 11, fitting the damper's dynamic viscous and equivalent stiffness to the piston's peak velocity yields a highly effective representation of the material's inherent nonlinearity. In Figure 11a, the equivalent stiffness of the damper demonstrates an initial slow increase, followed by a rapid escalation as piston velocity intensifies, signifying a nonlinear correlation between equivalent stiffness response and piston velocity. The gradual increase in equivalent stiffness at lower speeds may be attributed to the fact that the material's rheological properties are not fully activated at lower shear rates. Conversely, at higher velocities, the growth rate of equivalent stiffness markedly accelerates, revealing that the shear thickening effect becomes considerably more pronounced under conditions of high shear.

Additionally, a comparative analysis of equivalent stiffness trends at different amplitudes reveals that the stiffness increases most rapidly at an amplitude of 3 mm. This suggests that, at larger amplitudes, the STF damper can more effectively harness its shear thickening properties to respond to greater external forces. As amplitude increases, the material inside the damper undergoes more substantial deformation, leading to significant microstructural changes and molecular rearrangements, thereby enabling the damper to exhibit greater stiffness under dynamic loading at higher amplitudes.

Simultaneously, in Figure 11b, the dynamic viscosity reveals a nonlinear relationship with piston peak velocity; however, its trend contrasts with that of the equivalent stiffness,

exhibiting a decrease as the piston peak velocity increases. This observation suggests that during the initial phase of velocity escalation, the dynamic viscosity of the STF material responds promptly, indicating that its internal structure can adapt swiftly to velocity variations at lower velocity thresholds, which leads to a pronounced reduction in dynamic viscosity. Nonetheless, as the piston peak velocity reaches a specific threshold, the rate of increase in the dynamic viscosity gradually diminishes, entering a more stable regime. Additionally, a comparative analysis of the dynamic viscosity trends at varying amplitudes indicates that, at lower amplitudes, the decline is most significant within the low-speed range, although the maximum dynamic viscosity is still observed at 1 mm.

Figure 11c illustrates the nonlinear relationship between friction force and piston peak velocity. At an amplitude of 1 mm, the friction force decreases as piston peak velocity increases. At an amplitude of 2 mm, the friction force initially decreases before increasing, while at an amplitude of 3 mm, the friction force continuously rises. This demonstrates that at higher amplitudes, the shear thickening characteristics of the STF material are fully activated. This sustained increase in friction force highlights the exceptional performance of the STF damper at larger amplitudes, allowing it to deliver effective energy dissipation and control across a broader range of velocities.

Figure 12 illustrates the force-displacement curves derived from both experimental measurements and theoretical calculations under varying frequencies and amplitudes. The figure clearly reveals that the force-displacement response undergoes significant changes as both amplitude and frequency increase. As the amplitude rises, the hysteresis loops expand, indicating greater energy dissipation. Similarly, an increase in frequency results in a broader force response within the hysteresis loops, signifying that the STF damper exhibits stronger damping characteristics under higher dynamic loads.

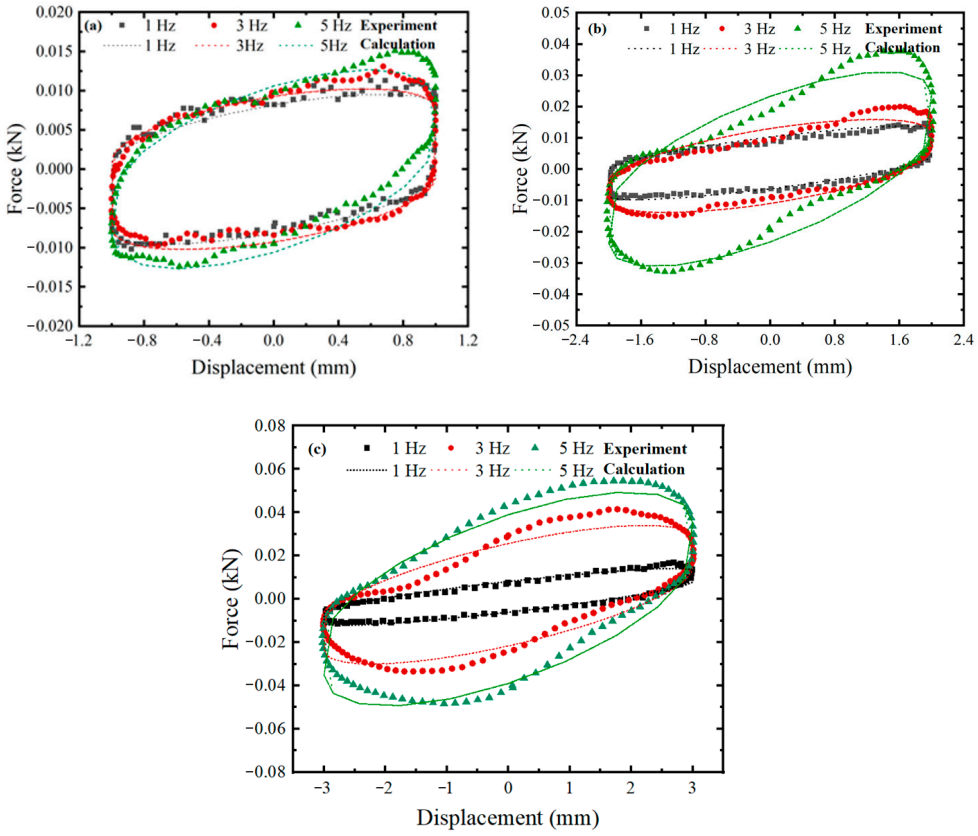

Figure 12. Force-displacement curves from both experiment and calculation under different frequencies and amplitudes. (**a**) STF damper, A = 1 mm (**b**) STF damper, A = 2 mm (**c**) STF damper, A = 3 mm.

As for the discrepancies between the experimental measurements and theoretical calculations, these deviations may partially stem from the compression and expansion of air within the damper. During dynamic loading, especially at higher frequencies, the behavior of the air may not have been fully captured by the theoretical model, resulting in the experimental data showing greater force variations than anticipated.

5. Conclusions

This study developed a self-adaptive STF material that rapidly and reversibly modifies its viscosity in response to shear rates, utilizing a 25% mass fraction of SiO_2 and a compounded polyethylene glycol solution (PEG200:PEG400 = 2:1). The study optimized and validated the design of the STF damper, demonstrating its significant potential in variable stiffness applications.

(1) The proposed STF material exhibits a pronounced shear thickening behavior, with a 412% increase in viscosity. This thickening initiates at a shear rate of 15.1 1/s and peaks at 30.1 1/s, beyond which the material transitions into a shear thinning state.
(2) Simulation results indicate that as the excitation frequency, excitation amplitude, and piston radius increase, the average shear rate of the STF in the annular gap region also gradually increases. When the piston diameter is 36 mm, the average shear rate of the STF material in the annular gap region does not exceed 30.1 1/s, ensuring that the STF material does not extensively enter the shear thinning stage when the damper is subjected to sinusoidal excitation within the range of 1–5 Hz and 1–3 mm.
(3) A STF damper was fabricated based on the optimized design. Experimental results showed that the stiffness of the STF damper varies with changes in excitation frequency. When the external frequency increases from 1 Hz to 5 Hz at an amplitude of 3 mm, the equivalent stiffness of the STF spacer increases from 3.2 N/mm to 9.1 N/mm, nearly tripling.

Author Contributions: S.C.: Conceptualization, Investigation, Writing—original draft; X.F.: Software, Methodology; P.M.: Formal analysis, Experiment; L.C. and L.W.: Validation; J.Y.: Funding. All authors have read and agreed to the published version of the manuscript.

Funding: This study is supported by the Science and Technology Research Program of Chongqing Municipal Education Commission (Grant No. KJZD-K202401505), and the Natural Science Foundation of Chongqing Science and Technology Commission (Grant No. QCSTB2023NSCQ-MSX0029).

Data Availability Statement: The data presented in this study are available from the corresponding author upon reasonable request.

Conflicts of Interest: The authors declare no conflicts of interest.

References

1. Zhang, Y.; Guo, J.; Yang, J.; Li, X. Recent Structural Developments and Applications of Magnetorheological Dampers (MRD): A Review. *Magnetochemistry* **2023**, *9*, 90. [CrossRef]
2. Li, H.; Li, L.; Hu, R.; Ye, M. Simplified design of nonlinear damper parameters and seismic responses for long-span cable-stayed bridges with nonlinear viscous dampers. *Front. Struct. Civ. Eng.* **2024**, *18*, 1103–1116. [CrossRef]
3. Mohtasim, S.M.; Ahammed, R.; Rahman, M.M.; Rashid, M.M.; Roy, R.; Aziz, M.A. Recent developments of regenerative magnetorheological (RMR) damper: A review. *Korea-Aust. Rheol. J.* **2021**, *33*, 201–224. [CrossRef]
4. Aziz, M.A.; Aminossadati, S.M. State-of-the-art developments of bypass Magnetorheological (MR) dampers: A review. *Korea-Aust. Rheol. J.* **2021**, *33*, 225–249. [CrossRef]
5. Deng, H.; Lian, X.; Gong, X. A brief review of variable stiffness and damping magnetorheological fluid dampers. *Front. Mater.* **2022**, *9*, 1019426. [CrossRef]
6. Chen, C.; Chan, Y.S.; Zou, L.; Liao, W.-H. Self-powered magnetorheological dampers for motorcycle suspensions. *Proc. Inst. Mech. Eng. Part D J. Automob. Eng.* **2017**, *232*, 921–935. [CrossRef]
7. Bastola, A.K.; Li, L.; Paudel, M. A hybrid magnetorheological elastomer developed by encapsulation of magnetorheological fluid. *J. Mater. Sci.* **2018**, *53*, 7004–7016. [CrossRef]
8. Cao, S.; Hu, F.; Zhang, G. Superelastic Shape Memory Alloy Honeycomb Damper. *Appl. Sci.* **2023**, *13*, 13154. [CrossRef]

9. Liu, H.; Fu, K.; Cui, X.; Zhu, H.; Yang, B. Shear Thickening Fluid and Its Application in Impact Protection: A Review. *Polymers* **2023**, *15*, 2238. [CrossRef]
10. Fu, K.; Wang, H.; Zhang, Y.X.; Ye, L.; Escobedo, J.P.; Hazell, P.J.; Friedrich, K.; Dai, S. Rheological and energy absorption characteristics of a concentrated shear thickening fluid at various temperatures. *Int. J. Impact Eng.* **2020**, *139*, 103525. [CrossRef]
11. Hasanzadeh, M.; Mottaghitalab, V. The Role of Shear-Thickening Fluids (STFs) in Ballistic and Stab-Resistance Improvement of Flexible Armor. *J. Mater. Eng. Perform.* **2014**, *23*, 1182–1196. [CrossRef]
12. Aşkan, A.; Çapkurt, M.; Acar, E.; Aydın, M. Influence of dispersion liquid and silica concentration on rheological properties of shear thickening fluids (STFs). *Rheol. Acta* **2023**, *62*, 447–460. [CrossRef]
13. Sun, L.; Liang, T.; Zhang, C.; Chen, J. The rheological performance of shear-thickening fluids based on carbon fiber and silica nanocomposite. *Phys. Fluids* **2023**, *35*, 032002. [CrossRef]
14. Madraki, Y.; Ovarlez, G.; Hormozi, S. Transition from Continuous to Discontinuous Shear Thickening: An Excluded-Volume Effect. *Phys. Rev. Lett.* **2018**, *121*, 108001. [CrossRef] [PubMed]
15. Fu, K.; Wang, H.; Chang, L.; Foley, M.; Friedrich, K.; Ye, L. Low-velocity impact behaviour of a shear thickening fluid (STF) and STF-filled sandwich composite panels. *Compos. Sci. Technol.* **2018**, *165*, 74–83. [CrossRef]
16. James, N.M.; Han, E.; de la Cruz, R.A.L.; Jureller, J.; Jaeger, H.M. Interparticle hydrogen bonding can elicit shear jamming in dense suspensions. *Nat. Mater.* **2018**, *17*, 965–970. [CrossRef]
17. Xu, Y.-l.; Gong, X.-l.; Peng, C.; Sun, Y.-q.; Jiang, W.-q.; Zhang, Z. Shear Thickening Fluids Based on Additives with Different Concentrations and Molecular Chain Lengths. *Chin. J. Chem. Phys.* **2010**, *23*, 342–346. [CrossRef]
18. Moriana, A.; Pérez-López, D.; Gómez-Rico, A.; Salvador, M.d.l.D.; Olmedilla, N.; Ribas, F.; Fregapane, G. Irrigation scheduling for traditional, low-density olive orchards: Water relations and influence on oil characteristics. *Agric. Water Manag.* **2007**, *87*, 171–179. [CrossRef]
19. Antosik, A.; Głuszek, M.; Żurowski, R.; Szafran, M. Effect of SiO_2 Particle Size and Length of Poly(Propylene Glycol) Chain on Rheological Properties of Shear Thickening Fluids. *Arch. Metall. Mater.* **2016**, *61*, 1511–1514. [CrossRef]
20. Gürgen, S.; Sofuoğlu, M.A.; Kuşhan, M.C. Rheological compatibility of multi-phase shear thickening fluid with a phenomenological model. *Smart Mater. Struct.* **2019**, *28*, 035027. [CrossRef]
21. Helber, R.; Doncker, F.; Bung, R. Vibration attenuation by passive stiffness switching mounts. *J. Sound Vib.* **1990**, *138*, 47–57. [CrossRef]
22. Laun, H.M.; Bung, R.; Schmidt, F. Rheology of extremely shear thickening polymer dispersionsa) (passively viscosity switching fluids). *J. Rheol.* **1991**, *35*, 999–1034. [CrossRef]
23. Gong, X.; Zhang, J.; Xuan, S. Multi-Functional Systems Based on Shear Thickening Fluid. In *Shear Thickening Fluid*; Springer: Cham, Switzerland, 2023; pp. 53–75. [CrossRef]
24. Sheikhi, M.R.; Gürgen, S.; Altuntas, O.; Sofuoğlu, M.A. Anti-impact and vibration-damping design of cork-based sandwich structures for low-speed aerial vehicles. *Arch. Civ. Mech. Eng.* **2023**, *23*, 71. [CrossRef]
25. Yay, Ö.; Diltemiz, S.F.; Kuşhan, M.C.; Gürgen, S. Shear Thickening Fluid-Based Vibration Damping Applications. In *Smart Systems with Shear Thickening Fluid*; Springer: Cham, Switzerland, 2024; pp. 59–69. [CrossRef]
26. Zhang, X.Z.; Li, W.H.; Gong, X.L. The rheology of shear thickening fluid (STF) and the dynamic performance of an STF-filled damper. *Smart Mater. Struct.* **2008**, *17*, 035027. [CrossRef]
27. Zhou, H.; Yan, L.; Jiang, W.; Xuan, S.; Gong, X. Shear thickening fluid–based energy-free damper: Design and dynamic characteristics. *J. Intell. Mater. Syst. Struct.* **2014**, *27*, 208–220. [CrossRef]
28. Srivastava, A.; Majumdar, A.; Butola, B.S. Improving the Impact Resistance of Textile Structures by using Shear Thickening Fluids: A Review. *Crit. Rev. Solid State Mater. Sci.* **2012**, *37*, 115–129. [CrossRef]
29. Galindo-Rosales, F.J.; Rubio-Hernández, F.J.; Sevilla, A. An apparent viscosity function for shear thickening fluids. *J. Non-Newton. Fluid Mech.* **2011**, *166*, 321–325. [CrossRef]
30. Brown, E.; Jaeger, H.M. Shear thickening in concentrated suspensions: Phenomenology, mechanisms and relations to jamming. *Rep. Prog. Phys.* **2014**, *77*, 046602. [CrossRef]
31. Wei, M.; Lin, K.; Guo, Q.; Sun, H. Characterization and performance analysis of a shear thickening fluid damper. *Meas. Control* **2019**, *52*, 72–80. [CrossRef]